Journal Pre-proofs

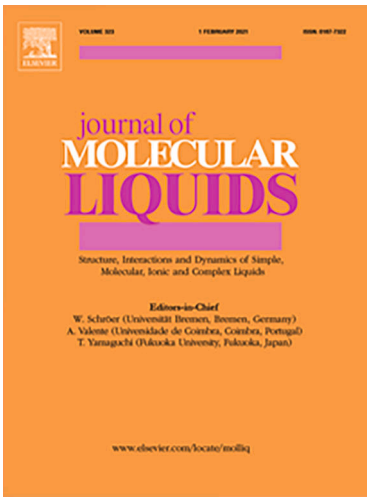

Incommensurate Lamellar Phase from Long Chain Mannosides: Investigation by X-Ray Scattering and Replica Exchange Molecular Dynamics (REMD)

Hockseng Nguan, Khairul Anwar Ishak, N. Idayu Zahid, Alfonso Martinez-Felipe, Rauzah Hashim, Nurul Fadhilah Kamalul Aripin

PII: S0167-7322(22)00565-7
DOI: https://doi.org/10.1016/j.molliq.2022.119027
Reference: MOLLIQ 119027

To appear in: *Journal of Molecular Liquids*

Received Date: 1 December 2021
Revised Date: 23 March 2022
Accepted Date: 25 March 2022

Please cite this article as: H. Nguan, K. Anwar Ishak, N. Idayu Zahid, A. Martinez-Felipe, R. Hashim, N. Fadhilah Kamalul Aripin, Incommensurate Lamellar Phase from Long Chain Mannosides: Investigation by X-Ray Scattering and Replica Exchange Molecular Dynamics (REMD), *Journal of Molecular Liquids* (2022), doi: https://doi.org/10.1016/j.molliq.2022.119027

Incommensurate Lamellar Phase from Long Chain Mannosides: Investigation by X-Ray Scattering and Replica Exchange Molecular Dynamics (REMD)

Hockseng Nguan[1], Khairul Anwar Ishak[2], N. Idayu Zahid[2], Alfonso Martinez-Felipe[3, 4], Rauzah Hashim[2]*, Nurul Fadhilah Kamalul Aripin[2,5]*

[1]Institute of Atomic and Molecular Sciences, Academia Sinica, P. O. Box 23-166, Taipei 10617, Taiwan.

[2]Centre for Fundamental and Frontier Sciences in Nanostructure Self-Assembly, Department of Chemistry, Faculty of Science, Universiti Malaya, 50603 Kuala Lumpur, Malaysia.

[3]Chemical Process and Materials Research Group, School of Engineering, University of Aberdeen, King's College, Aberdeen AB24 3UE, UK.

[4]Centre for Energy Transition, University of Aberdeen, King's College, Aberdeen AB24 3UE, UK.

[5]School of Chemical Engineering, College of Engineering, Universiti Teknologi MARA, 40450 Shah Alam, Malaysia.

*Corresponding authors

Email address: fadhilah9413@uitm.edu.my, Phone number: +603-5543 8415

Email address: rauzah@um.edu.my

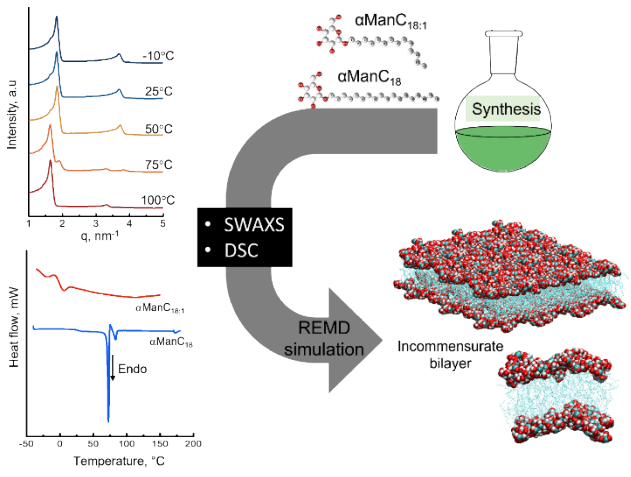

Graphical Abstract

Abstract

We report the synthesis and phase behaviour of two anhydrous mannosides ($\alpha ManC_{18}$ and $\alpha ManC_{18:1}$) with stearyl and monounsaturated oleyl hydrocarbon chains that can be obtained from vegetable sources. These mannosides have been characterised by differential scanning calorimetry, polarised optical microscopy and small- and wide-angle X-ray scattering. The two compounds exhibited multiple *d*-spacing bilayer structures. $\alpha ManC_{18:1}$ gives a distinct incommensurate lamellar that persists until high temperature. On the other hand, $\alpha ManC_{18}$ forms an incommensurate gel phase only at low temperature but undergoes a transition into the lamellar (L_α) liquid crystal phases on heating. The results were confirmed by replica exchange molecular dynamics (REMD). The average hydrocarbon chain/headgroup tilt angles $\langle\phi\rangle/\langle\theta\rangle$, and average chain bending angle $\langle\psi\rangle$ were calculated for the simulated bilayer systems at ~25°C. The multiple averaged headgroup tilt angles $\langle\theta\rangle$ explain the observed incommensurate bilayer structures with different bilayer thicknesses in these long hydrocarbon chain of mannosides. Moreover, different tilting angles of the headgroup result in different surface areas per lipid. Relating the incommensurate phase properly to molecular parameters is important especially in multi-component membranes, where the interplay of different molecule types is difficult to predict on intuitive grounds.

Keywords: Glycosides; Mannosides; Incommensurate phases; REMD simulations; Oleyl Mannoside; Stearyl Mannosides

1. Introduction

The presence of small amounts of unsaturated lipids can have great impact on phase behaviour of biological membranes forming bilayers [1]. While *trans* unsaturated lipids are closely packed, a kinked *cis* double bond in the lipid chain disrupts the intra- and inter-molecular van der Waals interactions in the region [2, 3]. Unsaturation in bilayers has been investigated on phospholipids, by considering the effect of the number [4] and position [5, 6] of the double bonds. In contrast, the effect of unsaturation on glycolipids is less studied, even though these are commonly found in Nature, for example, in thylakoid cell membranes [7]. A glycolipid consists of a hydrophilic sugar head whose OH groups form hydrogen bonds with neighbouring sugar groups. Consequently, the headgroup region forms a network of hydrogen-bonded layer. Each sugar head is covalently linked to a hydrophobic hydrocarbon chain. The combination of hydrogen-bonding and non-polar interactions yields both rich thermotropic (in bulk) and lyotropic (in the presence of solvents) liquid crystalline behaviour, including lamellar, hexagonal, or complex three-dimensional cubic phases [8-21].

Molecular dynamics (MD) simulations can unveil complex phenomena of lipids and glycolipids, such as, raft formation [22-24], self-assembly [25], and interactions with membrane components [26-28]. Recently, we have observed that substitution of the 1→4 with 1→6 glycosidic linkage within the headgroup significantly decreases bilayer spacing and modifies the pattern of inter-headgroup hydrogen-bonding [17]. Introducing branched lipid chains, on the other hand, alters the interactions of the lamellar assembly, resulting into more fluid-like hydrophobic regions [17], and thus promotes polymorphism from columnar to smectic phases in Guerbet maltosides [29]. Recently, an improved and optimised simulation technique based on replica exchange molecular dynamics (REMD) has been developed and may be used for such challenging and computationally intensive problems [30-33].

In the present work, we study in detail two long-chain mannosides containing stearyl and oleyl chains, $\alpha ManC_{18}$ and $\alpha ManC_{18:1}$, respectively (see Figure 1). Mannose is a simple sugar, which can be naturally found in fruits like cranberry. It is an epimer of glucose and has important therapeutic value to treat glycosylation-deficient patients and selective bacterial infections [34, 35]. Mannoside derivatives are reported to have good antibacterial and anti-viral properties, that have become a growing interest to explore their potential for non-antibiotic treatment in urinary tract infections [36] and anti-viral drugs for HIV treatments [37], respectively. Stearyl and oleyl fatty esters, on the other hand, are lipid components from palm oil. Thus, even though $\alpha ManC_{18}$ and $\alpha ManC_{18:1}$ (Figure 1) are synthetic molecules, both derive

from Natural products. These sustainable surfactants have potential broad applications in the pharmaceutical and biological applications.

Our aim is to study interactions at the atomic level that can explain the role of the mannose headgroup and the alkyl chains (saturated and unsaturated) on the formation of lamellar structures in these glycosides in the anhydrous state, which provide basic understanding of the material in its pure state. To achieve this, DSC and SWAXS measurements were applied to determine the self-assembly properties, while both conventional atomistic MD and REMD simulations were used to verify the experimental findings. Taking advantage of the powerful simulation methodology, we also extracted detailed angular conformations of these lipids, namely, the headgroup, $\langle\phi\rangle$ and chain, $\langle\theta\rangle$ tilting angles as well as the chain bending, $\langle\psi\rangle$ angle. The headgroup tilting angle has also been studied by MD simulations [38]. A combination of such studies will unveil important correlations between molecular parameters and self-assembly in these new glycosides.

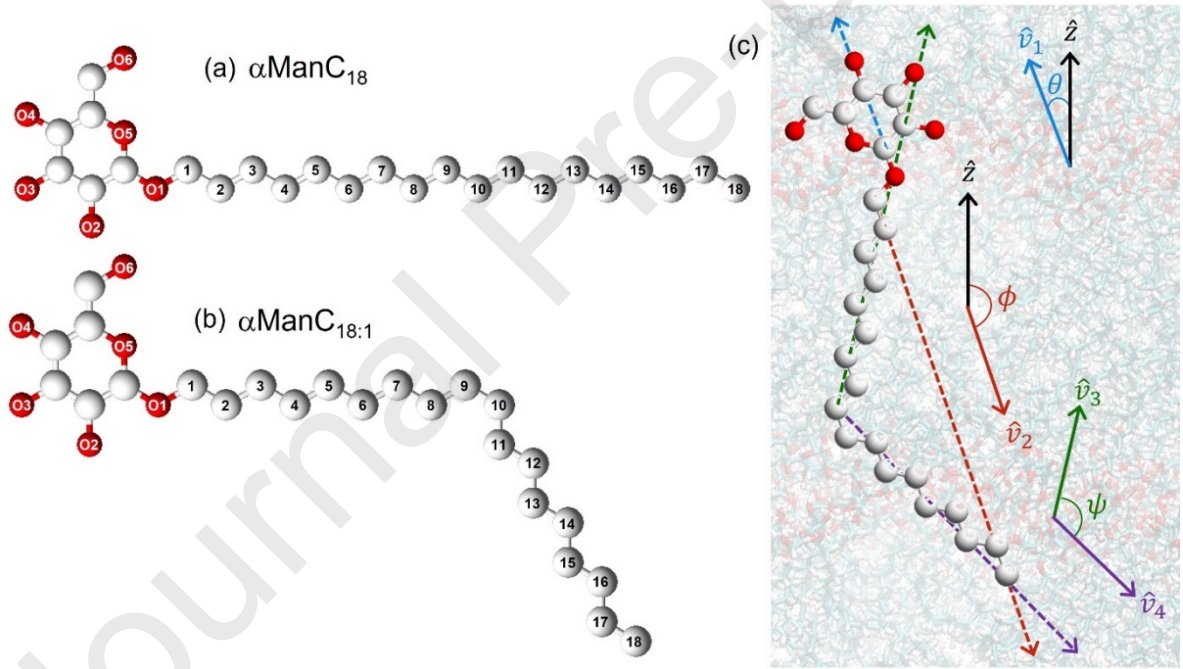

Figure 1. Molecular structures of $\alpha ManC_{18}$ and $\alpha ManC_{18:1}$ are shown in (a) and (b), respectively. In $\alpha ManC_{18:1}$ structure, between C9 and C10 exists a double bond, which is not shown in the drawing. (c) gives a schematic drawing to illustrate how the angles are defined. θ, is the angle between the vector $\hat{v}_1$ of atom O1 to O4, to the bilayer normal ($\hat{z}$) and hence $\theta = \cos^{-1}(\hat{v}_1 \cdot \hat{z})$, $\phi = \cos^{-1}(\hat{v}_2 \cdot \hat{z})$, where $\hat{v}_2$ is the vector from C1 to C18 and ψ, is as $\psi = \cos^{-1}(-\hat{v}_3 \cdot \hat{v}_4)$, where $\hat{v}_3$ and $\hat{v}_4$ represent the unit vectors pointing from C9 to C1 and C9 to C18, respectively. ψ is defined in such a way that the more bent is the chain, the bigger its

value.

2. Experimental procedure

2.1. Materials preparation

All chemicals used in the synthesis of $\alpha ManC_{18}$ and $\alpha ManC_{18:1}$, D(+)-mannose monohydrate and boron trifluoride diethyl etherate, $BF_3.O(C_2H_5)_2$, were purchased from Sigma Aldrich, while acetic anhydride, 1-octadecanol and *cis*-9-octadecen-1-ol were purchased from Merck. Solvents for synthesis were analytical grade. All chemicals and solvents were used without further purification.

2.2. Synthesis

The mannosides, $\alpha ManC_{18}$, and $\alpha ManC_{18:1}$, were synthesised using a three-steps method consisting of peracetylation, glycosylation, followed by deacetylation. The detailed synthetic procedure is described in the electronic supplementary information (ESI, section 1) and the chemical structures of $\alpha ManC_{18}$, and $\alpha ManC_{18:1}$, were confirmed by ^{1}H-NMR spectroscopy, using a Bruker NMR Systems spectrometer at 400 MHz (see Figure ESI1 and ESI2).

2.3. Characterisation techniques

Polarised optical microscopy (POM) and differential scanning calorimetry (DSC) were used to determine the phase behaviour of the mannosides. The textural analysis was carried out using an Olympus BX51 microscope equipped with cross-polarising filters coupled to a Mettler Toledo FP82HT hot stage. Samples for POM analysis were placed between two glass slides, heated to their respective isotropic phases, and cooled down to room temperature prior to the analyses. DSC measurements were performed in subsequent heating and cooling cycles, ranging from –40°C to above their respective clearing temperatures, at rates of ±5°C/min, using a Mettler Toledo differential scanning calorimeter 822e equipped with a Haake EK90/MT intercooler. Preparation of DSC samples involved drying in a vacuum oven at 50°C for at least 3 h in the presence of diphosphorus pentoxide, before placing the samples in 40 µl-sized aluminium pans for the measurements.

Small- and wide-angle X-ray scattering (SWAXS) was used to determine the repeat distance of the self-assembly of the sample. The small-angle region probes larger molecular assembly structures with dimensions typically between 1–100 nm. Whereas the wide-angle scatterings provide complementary information of the structure at the atomic length scale

between 0.1–1 nm [39, 40]. Thus, the bilayer *d*-spacing is obtained from the small-angle region, while those at wide-angle typically give an interplanar distance of the lipid chain packing.

SWAXS experiments were conducted using an Anton Paar SAXSpace equipped with a DX-Cu 12×0.45 SERFERT X-ray tube generating CuKα radiation with wavelength, λ = 0.1542 nm at 40 kV and 50 mA. The Goebel-mirror-focused and Kratky-slit-collimated X-ray beam was line-shaped (17 mm horizontal dimension at the sample). The scattered radiation from the samples measured in the transmission mode was recorded on a one-dimensional Dectris MYTHEN-1k microstrip solid-state detector. The *q*-range of the setup extends from 0.1 to 20.0 nm^{-1} at a sample-to-detector distance of 121 mm, where q is the scattering vector given by $q = 4\pi(\sin\theta)/\lambda$, 2θ is the scattering angle with respect to the incident beam, and λ is the wavelength of the X-ray beam. Silver behenate, which has a *d*-spacing of 5.84 nm (where $d = 2\pi/q_1$ is the lamellar spacing obtained from the position of the first-order reflection q_1), was used as a standard. Samples were dried in a vacuum oven at least for 48 h at 30°C before being placed inside a paste cell sample holder. The SWAXS measurements were run at various temperatures using a temperature-controlled sample stage (TCStage 300) within an accuracy of ±0.1°C. For $\alpha ManC_{18}$, the SWAXS patterns were obtained on heating at T= –10, 25, 50, 75, and 100°C, whilst for $\alpha ManC_{18:1}$, the patterns were attained at T= –10, 25, and 100°C. Prior to the measurements, the mannosides were first heated, then cooled down to –10°C; $\alpha ManC_{18}$ was heated above its clearing temperature, T~173°C, and $\alpha ManC_{18:1}$ at T= 150°C. All samples were thermally equilibrated for 5 min at each temperature before measurements. Data were calibrated by normalising the primary beam using SAXStreat software. The liquid crystal phases and the corresponding *d*-spacing were determined using SGI software (Space Group Indexing, V.03.2012). Data were analysed using the software package OriginPro 8.5, version 2010.

2.4 Computational methodology

Model construction

The initial coordinates of $\alpha ManC_{18}$ and $\alpha ManC_{18:1}$ were constructed and geometrically optimised using the Avogadro modelling software package [41]. Oxygen atoms in the headgroup and carbon atoms in the tail, are labelled as shown in Figure 1. An in-house program, written in FORTRAN, was then used to arrange the molecules in 8 × 8 monolayers. Each monolayer was geometry optimised, rotated by 180° and shifted to form a bilayer with the tail

group of the molecules pointing toward each other at the centre of the bilayer, and the headgroups facing opposite directions. The resulting simulation cells contained 128 lipids (64 per leaflet) without water, to represent the anhydrous single bilayer system.

Simulation details

The initial bilayer structures were applied as starting configurations for the subsequent MD simulations, where their intra- and intermolecular interactions were defined by a complete atomistic force field of CHARMM36 [26, 42, 43]. These systems were simulated over a time of 400 ns in the isothermal-isobaric NpT simulation at 25°C.

A simulation system with a rough potential energy surface with several local minima, depends on its initial structure. Thus, a different starting configuration will lead the system to a different local minimum. There are a number of techniques to prevent the simulation run from being trapped in a local minimum, such as the conformational flooding technique [41] and replica exchange molecular dynamics (REMD) [30]. In this work, the REMD technique was used, where the ordinary MD system propagation is combined with the Monte Carlo replica exchange [42, 43], such that the low temperature structure can be frequently exchanged with the high temperature structure. The input structure for the subsequent REMD temperature simulation was the last structure snapshot of the NpT simulations. REMD requires a series of simulations at different temperatures running in parallel. The series of temperatures was chosen such that the potential energy distribution of each temperature run overlaps with those of its neighbouring temperature runs. For our REMD simulations, the number of replicas was 12, ranging from T= 20 to 87°C (namely, 20.00, 25.49, 31.10, 36.84, 42.70, 48.68, 54.79, 61.01, 67.10, 73.36, 80.39, and 87.01°C). The chosen temperatures of these replicas were determined using a C++ program developed by Yang et al. [44] and the exchange probability is 0.07. The exchanges between neighbouring replicas were checked every 1 ps, which is sufficient to compare the coupling times of the heat bath. Hence, there were 400,000 replica exchanges during the simulation. The data were collected every 20 ps.

The GROMACS version 5.0.1 [45, 46] was applied to our simulation in which the semi-isotropic pressure was maintained at 1 bar by using the Parrinello-Rahman pressure barostat of 5 ps relaxation time and 4.5×10^{-5} bar^{-1} compressibility [47]. The temperature was maintained by the Nose-Hoover thermostat of 0.1 ps relaxation time. Periodic boundary condition (PBC) has been applied to simulate the bulk liquid crystal phase [48]. In lipidic simulation, PBC is usually applied to a single bilayer of hydrated systems. Recently many simulations of a single

bilayer with low hydration also applied PBC [28, 49]. Therefore, in the present study we have utilised PBC to an anhydrous single bilayer. However, when simulating the anhydrous lipid system with PBC, Doxastakis et al. suggested that the multi-bilayer configuration is preferable (to a single bilayer) due to a reduction of coupling along the bilayer normal [50]. For comparison, we have also run MD simulations of double bilayer systems and the differences between the single and double bilayer systems were relatively insignificant (Δ=1.3% and 1.4%). The detailed comparison is given in electronic supplementary information (see ESI, section 3 and Figure ESI3). The atomic motions were propagated through the leap-frog algorithm [51], while all the bonds are constrained by using the LINCS algorithm truncated after the fourth order [52]. A time-step of 2 fs was used. Electrostatic interactions were treated by Particle-Mesh Ewald (PME) [53] of 1.6 Å Fourier mesh spacing, using a fourth-order interpolation with a cut-off of 12 Å. Meanwhile, the non-bonded interactions have a cut-off of 12 Å. The long-range dispersion correction was applied on energy and pressure.

3. Results and discussionD

3.1 Phase behaviour and structure

3.1.1 Differential scanning calorimetry (DSC)

The phase behaviour of $\alpha ManC_{18}$ and $\alpha ManC_{18:1}$ was studied from their DSC thermograms obtained from second heating scans, shown in Figure 2. Their transition temperatures and the corresponding enthalpies are extracted from the thermal profiles and are summarised in Table 1.

For $\alpha ManC_{18}$, a step-like peak associated with the glass transition temperature (T_g) was discernible at 28°C. Above the T_g, a sharp endothermic peak observed at 72ºC can be attributed to the melting of a solid gel phase (L_β), as previously reported [54]. On further heating, exothermic and endothermic peaks were observed at ~75°C and 83°C (respectively), associated to devitrification/recrystallisation and melting transitions of a liquid crystalline phase (Figure 2). A similar solid-to-liquid crystalline phase transition was reported in β-stearyl glucoside ($\beta GluC_{18}$)[54]. However, in that system, multiple crystal-to-crystal transitions were detected prior to entering the liquid crystal phase [54], while only a single crystal transition was observed in $\alpha ManC_{18}$.

On cooling under POM, $\alpha ManC_{18}$ exhibits a focal conic fan texture suggesting a lamellar phase, L_α (see Figure ESI4a). The high clearing transition observed at T_c=173°C from the DSC

thermogram compared to others *n*-alkyl α-mannosides ($6 \leq n \leq 14$, with T_c ranging between 85–163°C) [55], is justified by the greater energy required to break interactions to form the isotropic phase upon chain elongation.

Whilst the DSC curve of $\alpha ManC_{18:1}$ only exhibits a single glass transition at T_g~0°C (see again Figure 2), we identified focal conic fan textures corresponding to L_α phases below ~150ºC (Figure ESI4b). The absence of other first order transitions at the DSC thermogram is attributed to a loosely packed bilayer resulting from the presence of a double bond in the alkyl chain [54]. Unsaturation in alkyl chains is known to destabilise glycosides bilayers, reducing their corresponding clearing temperatures (for examples, $\beta GluC_{18:1}$ and $\beta GalC_{18:1}$ by ΔTc ~-20ºC, as compared to their stearyl counterparts; $\beta GluC_{18}$ and $\beta GalC_{18}$) [56-59].

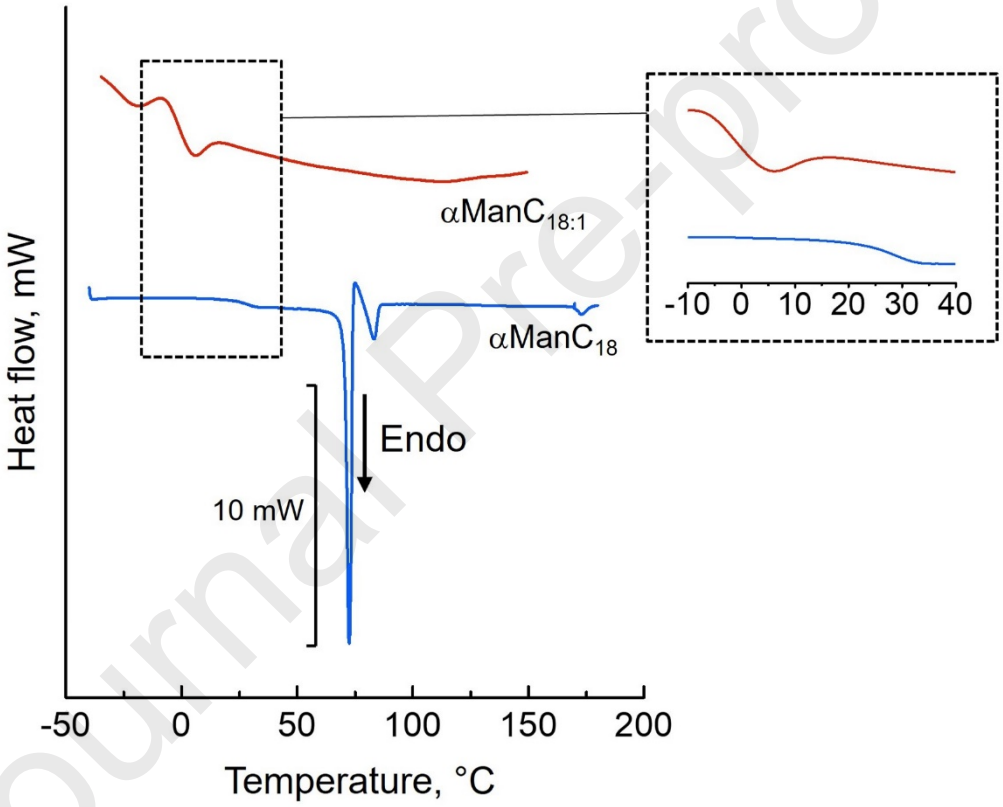

Figure 2. DSC curves of $\alpha ManC_{18:1}$ (top) and $\alpha ManC_{18}$ (bottom) corresponding to their second heating scans. The inset highlights the T_g of the mannosides. In these graphs, curves have been rescaled and shifted along the y-axis.

Table 1. Thermal properties of $\alpha ManC_{18}$ and $\alpha ManC_{18:1}$ obtained using differential scanning calorimetry. Error in the measured temperature is <1°C, whereas error in the enthalpy is <0.1 kJ·mol^{-1}

Mannosides	T_g, (°C)	T_m, (°C)	ΔH_m*, (kJ·mol^{-1})	T_c, (°C)	ΔH_c*, (kJ·mol^{-1})
$\alpha ManC_{18}$§	28	83	4.1	173	1.1
$\alpha ManC_{18:1}$	~0	-	-	-	-

*ΔH_m and ΔH_c are enthalpies associated with melting and clearing transitions, respectively.

§Between T_g and T_m, a sharp endothermic peak and an exothermic peak were observed at 72 and 75°C, respectively.

3.1.2 Small- and wide-angle X-ray scattering (SWAXS)

Figure 3 shows the scattering pattern of $\alpha ManC_{18}$ at small- and wide-angle regions measured at T= –10, 25, 50, 75, and 100 °C, and the respective *d*-spacings (bilayer thickness) are tabulated in Table 2. The measured temperatures were selected according to transition points observed in the DSC thermograms. In general, the small-angle X-ray scattering (SAXS) region of $\alpha ManC_{18}$ exhibited equidistant peaks that are characteristic of lamellar structures. All the scatterings at $q < 2.0$ nm^{-1} appear to have a shoulder (see Figure 3b), which will be discussed later.

The wide-angle X-ray scattering (WAXS) region of $\alpha ManC_{18}$ below T_m (–10, 25, and 50 °C) shows a symmetric sharp peak (Figure 3a), associated to the formation of an ordered lamellar phase with alkyl chains adopting an all-*trans* configuration [60, 61]. At T= –10 and 25 °C, this symmetric sharp peak was observed at q~15.3 nm^{-1} with a *d*-spacing of 0.41 nm, and at 50 °C, this peak shifted slightly to q~15.0 nm^{-1}, with a corresponding *d*-spacing of 0.42 nm. The peak can be attributed to the formation of a gel phase, where alkyl chains are packed in a hexagonal lattice ordering [61-63]. When the temperature was increased to T= 75 °C (> T_g), the strong peak in the WAXS region of $\alpha ManC_{18}$ disappeared, and two very weak peaks appeared at q~14.5 and 15.9 nm^{-1}, with *d*-spacing of 0.43 and 0.40 nm, respectively (Figure 3a). These changes indicate a transition from the gel phase to the less ordered liquid crystalline phase, previously observed in the DSC curves. On further heating to T= 100 °C, $\alpha ManC_{18}$ forms a lamellar liquid crystalline phase, as evidenced by a broad peak centred at q= 12.8 nm^{-1} (d= 0.49 nm) (Figure 3a).

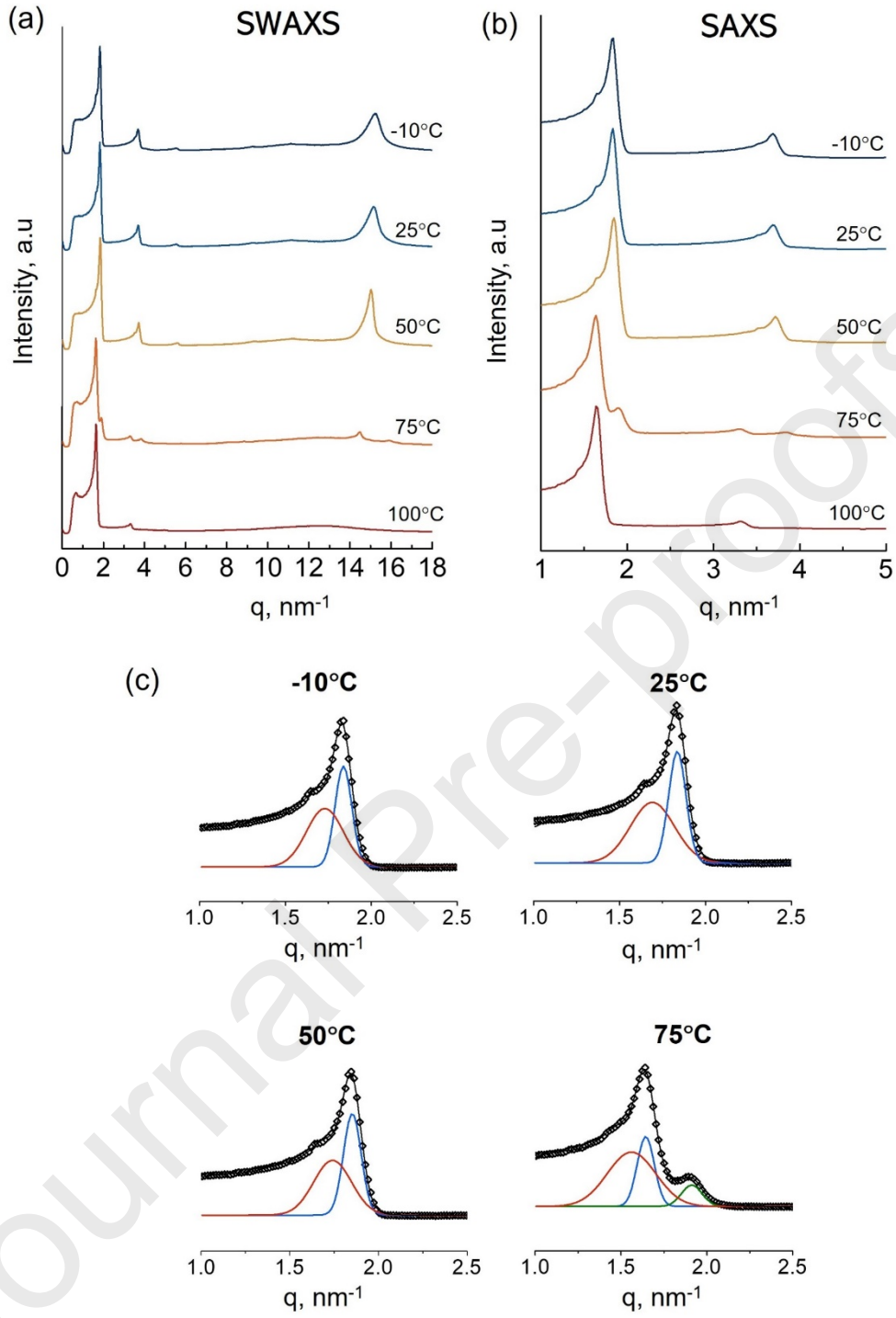

Figure 3. (a) SWAXS patterns of $\alpha ManC_{18}$ at T= –10, 25, 50, 75 and 100 °C obtained on heating while (b) highlights scatterings at the small-angle region. In (c), multiple peak fitting of the shoulder peak into its constituent peaks at all temperatures is shown. Curves in (a) and (b) are arbitrarily shifted along the y-axis.

The presence of the shoulder in the small-angle region of $\alpha ManC_{18}$ (q< 2.0 nm^{-1}, see Figure 3b) could be associated to multiple lamellar arrangements. Multiple peak fitting of the peak to several individual contributions is shown in Figure 3c, and their corresponding *d*-spacing values are tabulated in Table 2. Whilst $\alpha ManC_{18}$ shows two distinctive spacings in the gel phase ($T< T_m$), its liquid crystalline phase ($T> T_m$) is characterised by three lamellar *d*-spacings.

The X-ray wide-angle scattering region of $\alpha ManC_{18:1}$, on the other hand, displayed broad diffuse peaks that indicate the formation of liquid crystalline order throughout the measured temperatures (Figure 4a). At temperatures below the glass transition, T= –10 °C, the broad peak at wide angles (q~13.8 nm^{-1}) denotes a glassy state with corresponding *d*-spacing of 0.46 nm, similar to that reported for β-dodecyl maltoside [60]. This is consistent with the well-known trend of amphiphilic compounds to form glassy phases that retain liquid crystalline phases on cooling, albeit with restricted inter/intramolecular motions due to the strong interactions within the headgroup region [64]. When the temperature increased to T= 25 °C, the glassy state prevailed, accompanied with a slight increase in the *d*-spacing (0.48 nm) promoted by the higher molecular mobility. Upon further heating to T= 120 °C, the peak becomes less defined and shifts to q= 13.1 nm^{-1} with a *d*-spacing value of 0.48 nm, due to the transition of $\alpha ManC_{18:1}$ into a L_α phase. Our WAXS scattering results suggest that the oleyl tail occupies a larger volume that disrupts lateral packing of the molecules, due to the presence of the *cis* unsaturation.

At all measured temperatures, the small-angle region of $\alpha ManC_{18:1}$ shows the presence of equidistant peaks consistent with the formation of lamellar phases. At low temperatures, the assigned glassy phase has a persisting lamellar structure, and will be defined as $L_{\alpha G}$. The presence of several overlapped contributions in Figure 4b was investigated by multiple peak fitting at different temperatures (see Figure 4c). The results are summarised in Table 2, consisting of: two distinguished $L_{\alpha G}$ peaks at T= –10 ^oC (*d*-spacings of 3.46 and 4.00 nm), three peaks at T= 25 ^oC (3.23, 3.42, and 3.67 nm), and only two contributions at T= 120 ^oC (3.19 and 3.44 nm). For this unsaturated lipid ($\alpha ManC_{18:1}$), the *d*-spacings tend to decrease on heating. Similar results were observed for the palm kernel oil-based mannoside, αManPKO, which suggested the co-existence of two lamellar phases [65]. To further correlate the occurrence of multiple *d*-spacings to the bilayer structure of our samples, we perform in the next section molecular simulation studies.

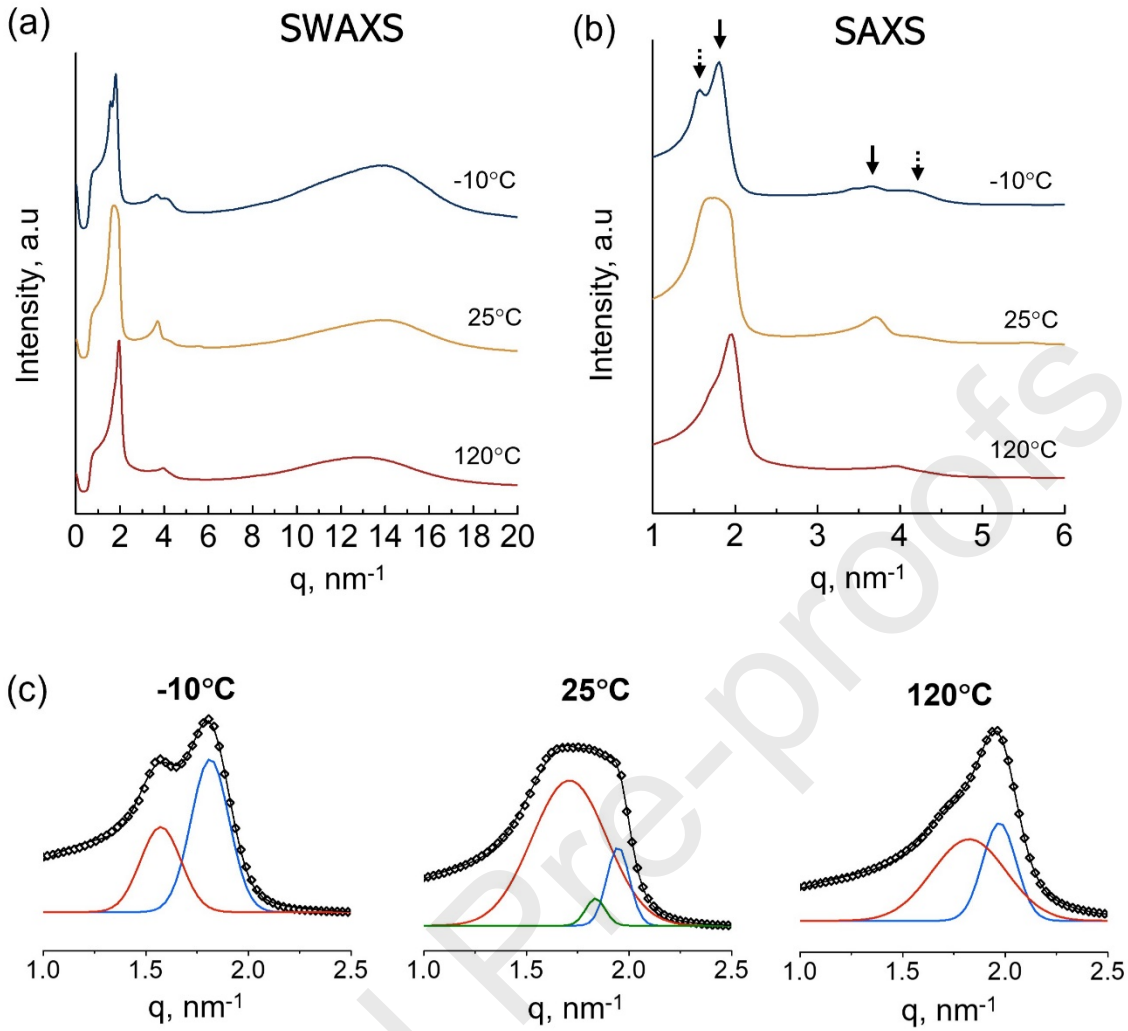

Figure 4. (a) SWAXS patterns of αManC$_{18:1}$ at T= −10, 25, and 120 °C, obtained on heating, where (b) highlights scatterings at the small-angle region and Bragg peaks denoted by arrows; (c) shows the multiple peak fitting of the SWAXS peak at T= −10, 25, and 120 °C, into its constituent contributions. Curves in (a) and (b) are arbitrarily shifted along the y-axis.

3.2 Molecular simulation

3.2.1 Bilayer thickness and distribution

Prior to performing the simulations, initial model structures for αManC$_{18}$ and αManC$_{18:1}$ were built based on their low-energy conformations. For the simulation of αManC$_{18}$, the starting configuration was constructed in such a way that the lipid chain consists of only all-*trans* alkyl chain (Figure 5a). During the simulation, these single bonds will be freely rotating to take all possible conformations. In the case of αManC$_{18:1}$, the lipid is modelled to contain

one double bond at C9, preventing free bond rotation between C9 and C10 carbons. This strategy generates two possible low-energy conformations as described by Rich [66], namely, the U-shaped conformation with the double bond in the most curved region, and the somewhat 'linear' conformation. In our simulation, we employed this 'linear' conformation in the lipid bilayer systems of $\alpha ManC_{18:1}$, to provide close comparison with $\alpha ManC_{18}$, and the minimised structure is shown in Figure 5b.

For the 400 ns simulations, the bilayer thicknesses of the two compounds at T= 25°C are given in Figure 5c, which shows that the bilayer spacing for $\alpha ManC_{18}$ and $\alpha ManC_{18:1}$ fluctuates around 3.6 nm. From 50 ns up to 400 ns, the bilayer spacings for $\alpha ManC_{18}$ and $\alpha ManC_{18:1}$ are 3.58 ± 0.03 and 3.55 ± 0.05 nm, respectively. These bilayer spacings lie within the range of those measured by SAXS (see Table 2). At all measured temperatures the X-ray *d*-spacings are less than twice the lipid lengths due to configurational isomerisation. It should be noted that the SAXS measurements for these compounds depict two or more *d*-spacings. However, our MD simulations only show a unique bilayer thickness obtained from the averaging process of the simulation run. Over the last 350 ns, the bilayers in $\alpha ManC_{18}$ and $\alpha ManC_{18:1}$ did not reach the thickness as low as 3.4 nm, observed experimentally (see the final MD bilayer configuration Figure ESI3). This suggest that there could be an energy barrier that prevents the bilayers to change from 3.6 nm to other significantly shorter spacing. If such barrier is significantly higher than the thermal fluctuation, longer simulation times would not help the layer thickness of the system to further evolve. Furthermore, calculating these energy barriers requires understanding the potential energy surfaces of these bilayer systems, and this is nontrivial.

To overcome the dependence of the simulation on the initial glycolipid structures, we applied REMD. At T= 25.49°C, the 400 ns REMD simulations evidence the formation of $\alpha ManC_{18}$ and $\alpha ManC_{18:1}$ bilayer spacings, as displayed in Figure 6a and 6c, respectively. Results in Figure 6a show that $\alpha ManC_{18}$ forms bilayers thickness ranging from 3.4 nm to 3.8 nm, while its final REMD bilayer configuration is given in Figure ESI5. Beyond 150 ns, the bilayer thickness distribution narrows down to two values: around 3.4 and 3.7 nm. The non-Gaussian plot in Figure 6b (blue curve) denotes a superposition of bilayer thickness distributions. At T= 25.49°C, two most dominant peaks in $\alpha ManC_{18}$ are observed at 3.45 and 3.65 nm (with ~5% error), which is in good agreement to the two bilayer thicknesses observed in the X-ray scattering pattern fitted at 3.42 and 3.72 nm (see Table 2). Simulation of $\alpha ManC_{18}$ at T= 48.68°C, on the other hand, resulted in a superposition of many Gaussian curves (see green curve in Figure 6b), with the main peak bilayer spacing at ~3.65 nm becoming more

dominant. This is in fair agreement with the SAXS results at T= 50°C, where the dominating bilayer had a thickness of 3.4 nm, Figure 3c. The high temperature simulation at T= 73.36°C produced a broad distribution of bilayer thickness peaked at 3.55 nm.

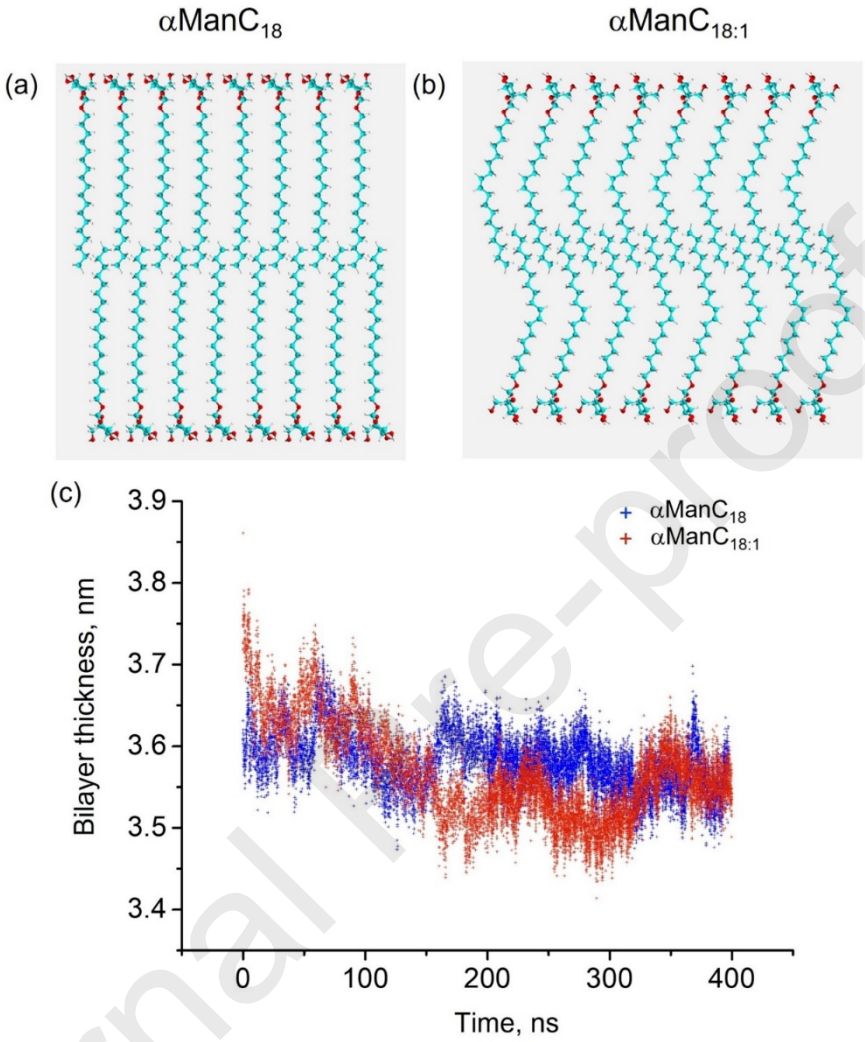

Figure 5. The MD simulation of $\alpha ManC_{18}$ and $\alpha ManC_{18:1}$ at T= 25°C; (a) side view of the initial guessed bilayer structure of $\alpha ManC_{18}$; (b) side view of initial guessed bilayer structure of $\alpha ManC_{18:1}$ with interdigitation; (c) bilayer thickness throughout 400 ns MD simulation of the two different initial structures.

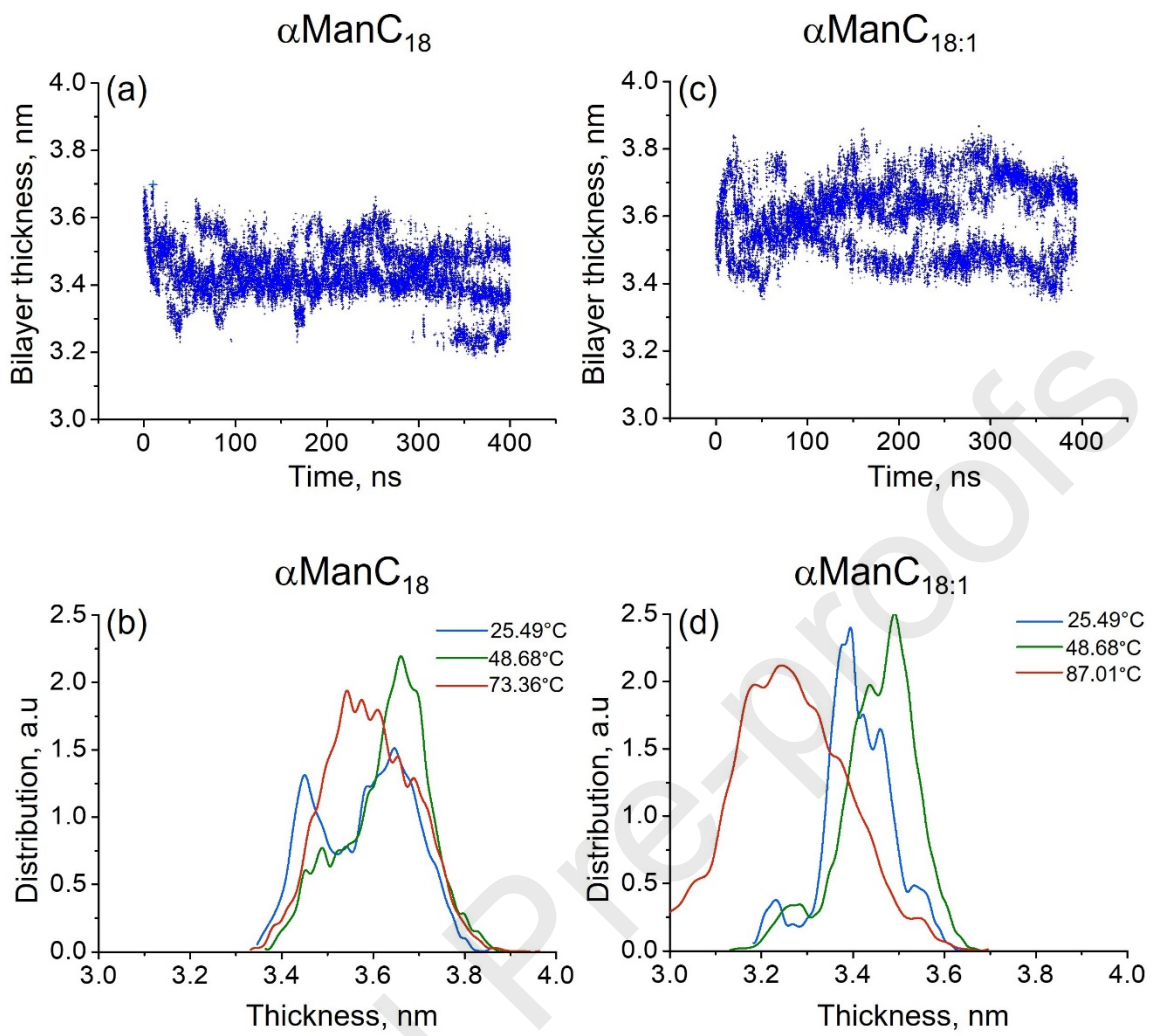

Figure 6. The REMD simulation results: bilayer thicknesses over the simulation time for: (a) $\alpha ManC_{18}$ and (c) $\alpha ManC_{18:1}$. Bilayer thickness distributions (from 400 ns frame) of: (b) $\alpha ManC_{18}$ at T= 25.49, 48.68, and 73.36°C; and (d) $\alpha ManC_{18:1}$, at T= 25.49, 48.68, and 87.01°C.

This result poorly matched the *d*-spacing from those measured by SAXS at T= 75°C (Figure 3c), whose small-angle scatterings after multiple peak fitting produce three bilayer thickness of 3.32, 3.82, and 4.03 nm. The bilayer thicknesses obtained from simulation are tabulated in Table 2. There are two possible reasons behind this apparent disagreement. On the one hand, REMD could not be suitable to simulate first order phase transition [68], which in this case occurred for $\alpha ManC_{18}$, as observed from the X-ray scatterings at T= 75°C (Figure 3b). A display of multiple sets of Braggs peaks usually indicates a transition of an ordered phase (non-crystalline) to a less ordered phase (lamellar phase). On the other hand, the forcefield could be limited to model the carbohydrate conditioned at high temperature. The CHARMM forcefield

[26, 42, 43] for carbohydrates was developed and tuned to match their crystalline and aqueous condense phase (at T= 25°C), therefore it might not perform well in the case of high temperatures.

Turning our attention to $\alpha ManC_{18:1}$, its REMD simulation at T= 25.49°C gives bilayer thicknesses ranging from 3.2 nm to 3.7 nm (see Figure 6c and Figure ESI5 for its bilayer final configuration). It should be noted that this range is wider and the minimum and maximum values of the bilayer thickness of $\alpha ManC_{18:1}$ are both lower compared to those of $\alpha ManC_{18}$ (Figure 6d). The corresponding average surface areas of headgroup per lipid (A) for both systems were found to be around A = 0.39 ± 0.01 nm^2, which is in the expected range for glycolipids (see Table ESI1) [17, 69-72]. However, the surface area per lipid presents different values (see Figure ESI6), implying that this averaged A value is not unique, which is consistent with the multi-d-spacing values of the bilayers reported above. Given the limitation of the small simulation system size, this observation may be indicative of incommensurate phases.

The distribution of the bilayer thicknesses in Figure 6c at T= 25.49°C is given by the blue curve in Figure 6d, with a maximum at d = 3.38 nm (main contribution), with two secondary peaks at d = 3.23 and 3.54 nm. The simulation provides a similar range of bilayer thicknesses with constituent peaks of d = 3.23, 3.42, and 3.67 nm, (see Figure 4c). At T= 48.68°C, the $\alpha ManC_{18:1}$ bilayer thickness distribution shows a major broad peak of around 3.50 nm (green curve in Figure 6d), suggesting that larger bilayer thicknesses are more dominant at higher temperatures. At the highest temperature of our REMD simulations, T= 87.01°C, the bilayer thickness of $\alpha ManC_{18:1}$ was broadly distributed and ranged from d= 3.0 nm up to 3.6 nm, with a maximum at 3.25 nm (see Figure 6d). If we project this result of T= 87.01°C to a higher temperature of T= 120°C, we expect that the distribution will remain as one broad peak because of the higher thermal fluctuation. Based on this projection, the REMD simulations seem not able to reproduce the $\alpha ManC_{18:1}$ bilayer thickness distribution at T= 120°C observed in the X-ray measurement. This again suggests the limitations of the forcefield at high temperatures.

Table 2. Thickness of the bilayers/*d*-spacings (*d*) of αManC$_{18}$ and αManC$_{18:1}$ obtained by SWAXS and REMD simulations. The *d*-spacing values of SWAXS are reported for the small-angle and wide-angle regions while in case of REMD, only *d*-spacing values at the small-angle region are reported. Error in the *d*-spacing measurements is <0.01 nm.

	SWAXS			REMD Simulation	
Compound	Temperature, °C	Bilayer thickness / *d*-spacings, nm		Simulated temperature, °C	Bilayer thickness / *d*-spacings, nm
		small-angle*	wide-angle		small-angle
αManC$_{18}$	–10	3.42, 3.63	0.41	-	-
	25	3.42, 3.72	0.41	25.49	3.45, 3.65
	50	3.40, 3.61	0.42	48.68	3.48, 3.65
	75	3.32, 3.82, 4.03	0.43 & 0.40	73.36	3.55[a]
	100	3.80	0.49	-	-
αManC$_{18:1}$	–10	3.46, 4.00	0.46	-	-
	25	3.23, 3.42, 3.67	0.46	25.49	3.23, 3.38, 3.54
	-	-	-	48.68	3.28, 3.45, 3.50
	-	-	-	87.01	3.25[b]
	120	3.19, 3.44	0.48	-	-

**d*-spacing values at small-angle region were obtained from multiple peak fitting of X-ray scatterings.

[a,b]*d*-spacing values obtained from the peak of the broad distributions.

In the following section, we investigate the simulated structures by examining the lipid tilting angles with respect to the bilayer normal, and the bending angle within the hydrocarbon chain. For a particular configuration the bilayer thickness depends on the headgroup and hydrocarbon chain tilting angles. A lower average headgroup and hydrocarbon chain tilting angles implies a larger bilayer thickness. Meanwhile, the average bending angle reflects on the ordering of the chain region, where higher bending angle means lower ordering. The sugar

headgroup is relatively rigid [73] compared to the hydrocarbon chain, therefore three angles were examined, namely the configurational average tilting angle of the headgroup $\langle\theta\rangle$, the tilting angle of the hydrocarbon chain $\langle\phi\rangle$ and the bending angle of the chain $\langle\psi\rangle$ (see Figure 1).

At T= 25.49°C, the REMD simulation results are in relatively good agreement with those obtained from the X-ray measurements (at T= 25°C). Therefore, we analyse the tilting and bending behaviours of the simulated bilayer systems at this temperature, where αManC$_{18}$ and αManC$_{18:1}$ give the gel phase and lamellar glassy phase, respectively. The configurational average tilting and bending angles ($\langle\theta\rangle_{MD}$, $\langle\phi\rangle_{MD}$ and $\langle\psi\rangle_{MD}$, and $\langle\theta\rangle_{REMD}$, $\langle\phi\rangle_{REMD}$ and $\langle\psi\rangle_{REMD}$) for MD (T= 25°C) and REMD (T= 25.49°C) simulations of αManC$_{18}$ and αManC$_{18:1}$, are shown in Figure 7, and the respective values are tabulated in Table 3.

3.2.2 Distribution of tilting and bending angles

The MD angular distributions of αManC$_{18}$ (Figure 7a) are narrower compared to those from the REMD simulation (Figure 7b). This implies that lesser bilayer thickness fluctuation (~0.2 nm) occurs during MD simulation compared to that in REMD (i.e., ~0.5 nm), (as seen in Figure 5c and 6a, respectively). Interestingly, the distribution profiles of chain tilting $\langle\phi\rangle_{REMD}$ (Figure 7b, red curve) and chain bending $\langle\psi\rangle_{REMD}$ (Figure 7b, green curve) obtained from the REMD simulations, are similar in shape to $\langle\phi\rangle_{MD}$ (Figure 7a, red curve) and $\langle\psi\rangle_{MD}$ (Figure 7a, green curve) obtained from MD, and their peak positions in both REMD and MD simulations are different by 2°. On the other hand, the headgroup tilting $\langle\theta\rangle_{REMD}$ distribution profile from REMD simulations shows two peaks (Figure 7b, blue curve), while that of MD shows one sole peak (Figure 7a, blue curve). The two peaks in $\langle\theta\rangle_{REMD}$ may be related to the two observed bilayer thicknesses in the REMD simulation (Figure 6a and 6b) and thus support the X-ray findings of two distinct bilayer spacings of αManC$_{18}$.

Similarly, the αManC$_{18:1}$ angular distribution from MD simulation (Figure 7c) are narrower than those of REMD (Figure 7d). For αManC$_{18:1}$, the MD chain tilting $\langle\phi\rangle_{MD}$ distribution (Figure 7c, red curve) has two peaks while the REMD counterpart only shows one peak (Figure 7d, red curve). On the other hand, the chain bending angle distributions from both MD ($\langle\psi\rangle_{MD}$) and REMD ($\langle\psi\rangle_{REMD}$) simulations have similar profiles and peak positions (see Figure 7c and 7d respectively, green curves). The αManC$_{18:1}$ headgroup tilting $\langle\theta\rangle_{REMD}$ distribution (Figure 7d, blue curve) shows three peaks, which differ from the $\langle\theta\rangle_{MD}$ distribution (Figure 7c, blue

curve), with only one peak. The multiple $\langle\theta\rangle_{REMD}$ peaks in αManC$_{18:1}$ correspond to the different bilayer thicknesses found in REMD simulations (see Table 2). This again suggests that the multiple bilayers thicknesses in αManC$_{18:1}$ are due to the headgroup arrangements, which have more than one distinct preferred tilting angle. For both compounds, the width of head tilting angle distributions $\langle\theta\rangle_{MD}$ are narrower compared to those distributions for $\langle\phi\rangle_{MD}$ and $\langle\psi\rangle_{MD}$, which implies that the headgroups fluctuate less (around 3.6 nm) during the MD simulations. The low fluctuation of the headgroup is due to the hydrogen bonds between headgroup that restricts their motion.

3.2.3 Average tilting and bending angles

The average chain bending angle $\langle\psi\rangle_{MD}$ for αManC$_{18}$ is 50.5° (Table 3), which is lower by 13° than that of the αManC$_{18:1}$. REMD also shows the same differential between the two compounds (see Table 3). These observations suggest that the presence of an unsaturated bond in the αManC$_{18:1}$ lipid tail increases significantly the average chain bending angle of the bilayer.

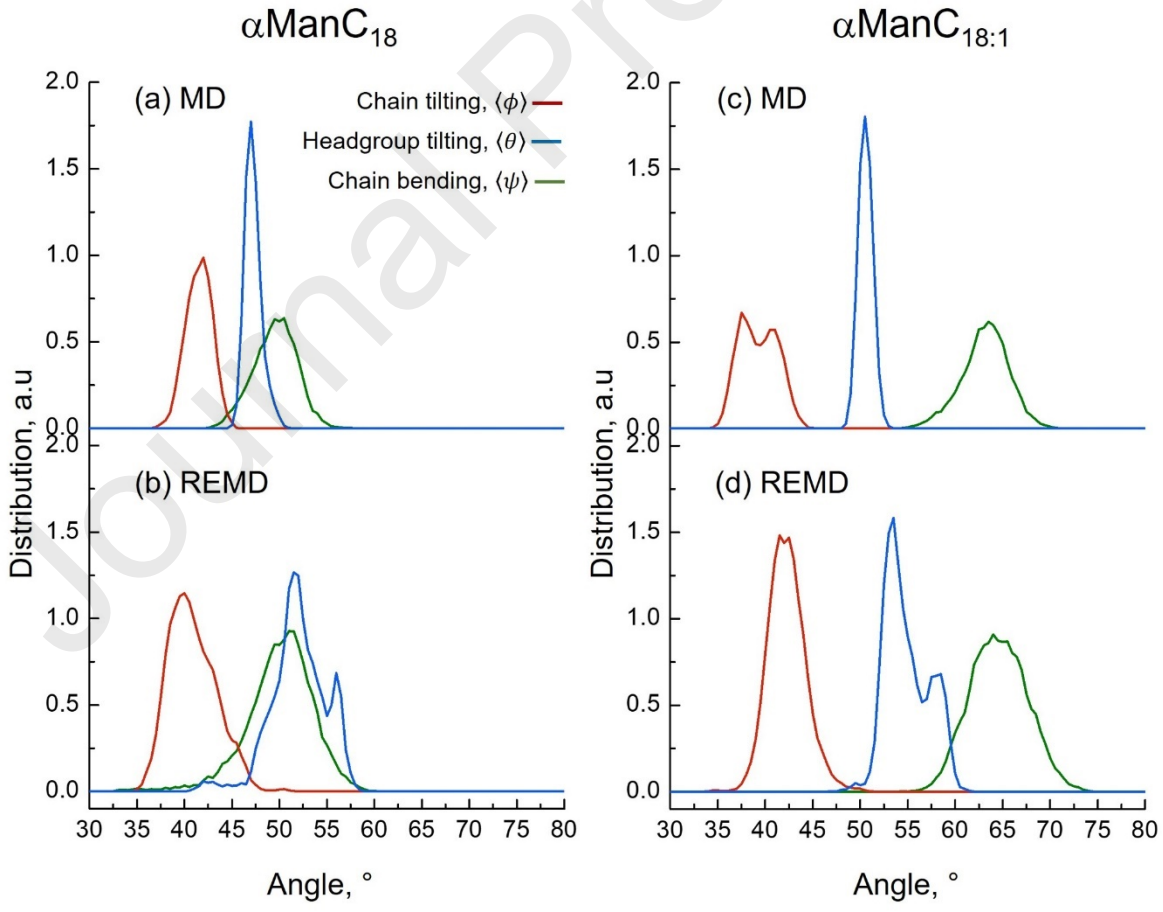

Figure 7. Distributions of average angles obtained from the MD and REMD simulations,

obtained at T= 25 and 25.49°C respectively, for αManC$_{18}$ and αManC$_{18:1}$: hydrocarbon chain tilting angle $\langle\phi\rangle$, (red curve); headgroup tilting angle $\langle\theta\rangle$, (blue curve); and hydrocarbon chain bending angle $\langle\psi\rangle$, (green curve).

Table 3. The calculated average hydrocarbon chain bending angle, $\langle\psi\rangle$, average hydrocarbon chain tilt angle, $\langle\phi\rangle$, and average headgroup tilt angle, $\langle\theta\rangle$, of αManC$_{18}$ and αManC$_{18:1}$ bilayers in the MD and REMD simulations at T= 25 and 25.49°C, respectively.

	MD simulation		**REMD simulation**	
	αManC$_{18}$	αManC$_{18:1}$	αManC$_{18}$	αManC$_{18:1}$
Average hydrocarbon chain bending angle, $\langle\boldsymbol{\psi}\rangle$ (°)	50.5	63.5	49.5, 51	64
Average hydrocarbon chain tilt angle, $\langle\boldsymbol{\phi}\rangle$ (°)	42	37.5, 41	40	41.5
Average headgroup tilt angle, $\langle\boldsymbol{\theta}\rangle$ (°)	47	50.5	51.5, 56	49.5, 53.5, 58.0

For αManC$_{18}$, the average chain tilting angle is $\langle\phi\rangle_{MD}$ = 42° (Table 3), while the presence of a double bond in αManC$_{18:1}$ results in two possible values for $\langle\phi\rangle_{MD}$ at 37.5 and 41° (Figure 7c). These unexpected double peaks could be due to an inadequate MD equilibration, since this peak almost disappears in the distribution plot of $\langle\phi\rangle_{REMD}$ (see Figure 7d). The average chain tilting angle in REMD for αManC$_{18}$ is 40° (Table 3).

The MD simulation gives average headgroup tilting angles of $\langle\theta\rangle_{MD}$ = 47.0 and 50.5°, for αManC$_{18}$ and αManC$_{18:1}$, respectively. In the REMD simulation, on the other hand, we report $\langle\theta\rangle_{REMD}$ = 51.5 and 56°, for αManC$_{18}$, while we found three peaks at $\langle\theta\rangle_{REMD}$= 49.5, 53.5 and 58.0°, for αManC$_{18:1}$ (Table 3).

3.3 Discussion on general phase behaviour of αManC$_{18}$ and αManC$_{18:1}$

Recent X-ray diffraction studies have reported incommensurate phases in block copolymers containing azobenzene derivatives [74] and non-symmetric dimesogens connected *via* hydrogen-bonding [75]. In the former, superposition diffractions of the primary peak were observed, while for the latter, the incommensurate phase was detected from the display of two sets of Bragg reflections, indicating a coexistence of smectic phases. Similar scattering patterns

as that of the azobenzene block copolymer have been observed for $\alpha ManC_{18}$ and $\alpha ManC_{18:1}$. For example, the SAXS scattering gives a shoulder below q= 2.0 nm^{-1}. Thus, we suggest that the long chain mannosides in the current study form incommensurate phases resulting from having inhomogeneous bilayer with different thickness in certain regions (see Figure 8). From the REMD simulations, the formation of incommensurate bilayer by the glycolipids is possible, as shown in Figure 8a. Incommensurate or frustrated phases in three dimensions have been described previously [76] and is thought to be the result of a competition between different characteristic length scales [77]. Frustrated behaviour in a thermotropic system is usually observed when the molecule contains a polar terminal group, such as a cyano group, where the competition is between the molecular length and the length of the anti-parallel molecular pairs to minimise the dipolar energy [78]. Another example of incommensurate phase occurs in a phospholipid monolayer, which is related to the headgroup ordering. In this case the frustration arise from different spatial requirements of aliphatic tails and headgroups [79, 80]. The resulting modulated phases with the tilt angle vary periodically along the surface.

In our present SWAXS analysis we have detected incommensurate phases when the mannosides were heated above their respective clearing temperature and cooled down to T= −10°C prior to measurement. Meanwhile, the cooling step is important to expedite molecular relaxation as the molecules slowly rearrange into the lowest level of free energy at room temperature. Samples that were cooled down to T= 25 °C do not show similar SAXS patterns. Additional REMD simulations support the SAXS findings at T ~25 °C, where multiple bilayer thicknesses were observed for both $\alpha ManC_{18}$ and $\alpha ManC_{18:1}$ (see Table 2).

From the angular analysis, chain tilting $\langle\phi\rangle$ and chain bending $\langle\psi\rangle$ are similar in value (within error) for both compounds. However, the headgroup tilting angles for both compounds show distinct behaviours. The REMD simulation for $\alpha ManC_{18}$ endows with two average headgroup tilting angles $\langle\theta\rangle$, which may cause the systems to exhibit double bilayer spacing (Figure 8b). While for $\alpha ManC_{18:1}$, there are three tilting headgroup angles producing three bilayer spacings as observed by SAXS (illustrated in Figure 8c). Long flexible hydrocarbon chains are necessary to provide a wide range of surface area of headgroup per lipid, so that the carbohydrate molecules can develop multiple tilting angles. Without such flexibility and variable surface area of headgroup per lipid, only one bilayer thickness is formed, such as short hydrocarbon chain glycolipids [65]. Nevertheless, as the temperature increase above the melting temperature, the incommensurate phase in $\alpha ManC_{18}$ becomes less obvious as the

molecules have more freedom to assemble with each other in a more uniform manner (Figure 8b). In contrast, due to the presence of the double bond in the lipid chain, the $\alpha ManC_{18:1}$

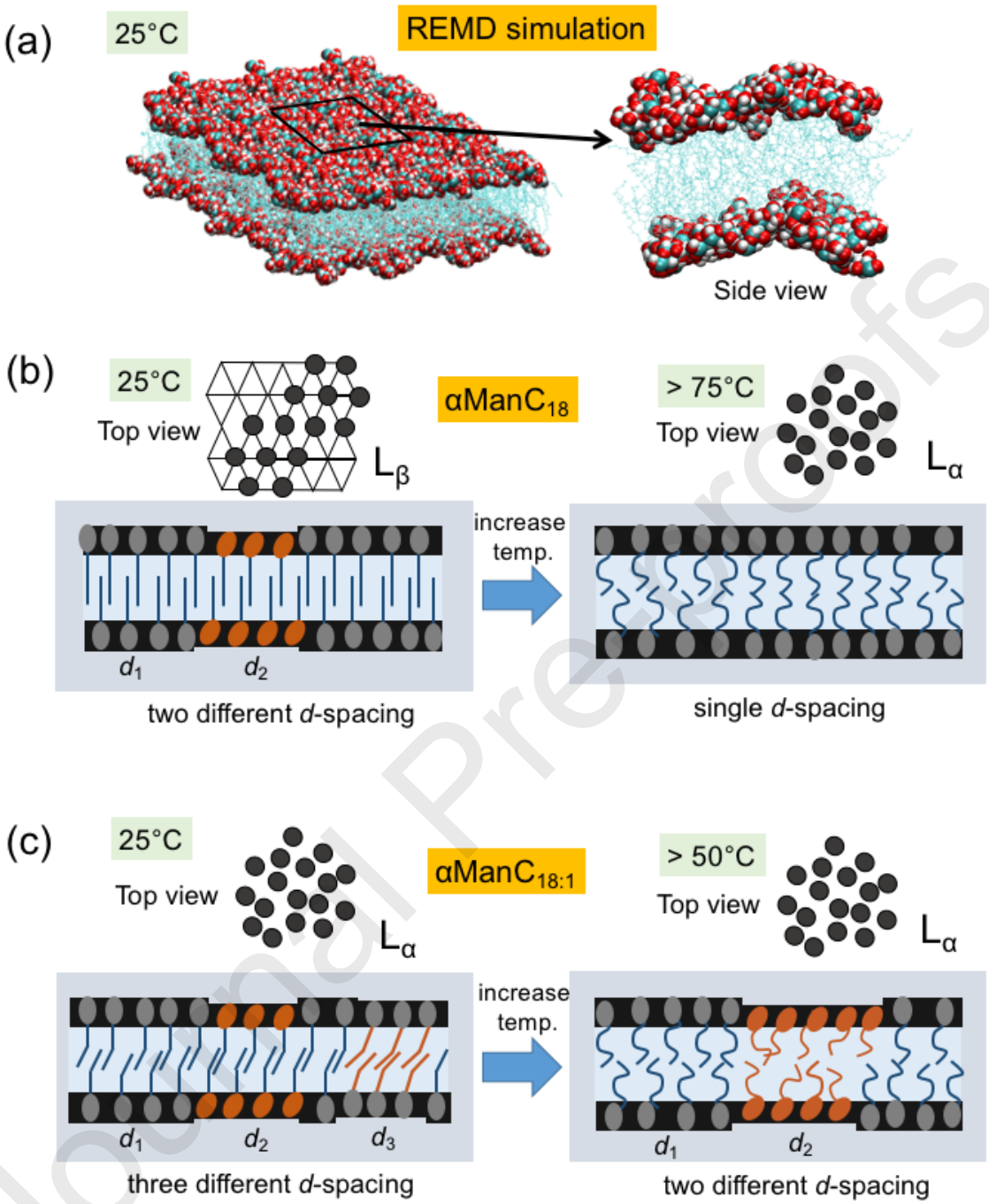

Figure 8. (a) A representation of the incommensurate bilayer at ambient temperature obtained from the REMD simulations, where the central box is replicated (9 times). Schematic phase behaviour with possible head or tail tilting (orange-coloured) that leads to the formation of the incommensurate phase in the self-assembly systems of (b) αManC$_{18}$ and (c) αManC$_{18:1}$.

molecule may easily get tilted in the system thus forming a bilayer with two average thickness (Figure 8c).

Previous simulations have been performed to calculate the tilting of lipid headgroups in 1,2-di-*O*-acyl-3-*O*-β-D-galactopyranosyl-*sn*-glycerol (MGDG) [38], which contains a galactose headgroup, hence a glycolipid, similar to our mannosides. Interestingly, they indicate that the galactose headgroup tilts at around 38° which is about 10° lower than those found in our mannoside systems (by REMD simulation). Given that the MGDG system is in a fully hydrated state, while the present studied systems are in dry state, the difference in angles is acceptable. Hence, the headgroup is more tilted in the dry state as compared to the hydrated state, due to the headgroup relaxation in the presence of water. It is clear that the degree of hydration is important in lipid membrane phenomena, and it may help understand membrane elastic stress and consequently membrane fluidity [81-84].

Lastly, it could be argued that the incommensurate phase reported here corresponds to a ripple phase ($P_{\beta'}$). P_{β}, normally observed in hydrated lipid bilayers of amphiphilic molecules, such as, dipalmitoylphosphatidylcholine (DPPC). The transition from gel to ripple phases is typically attributed to a decrease in chain tilting on heating, whereas hydration and mobility of the headgroup tend to increase. The absence of sawtooth-shaped SAXS scatterings in the vicinity of the main lamellar peaks [85, 86], however, seems to discard the formation of the P_{β} phase in our mannosides, which is also consistent with their anhydrous character.

Conclusion

The two mannose-based glycosides, $\alpha ManC_{18}$ and $\alpha ManC_{18:1}$, exhibited multiple bilayer structures at various selected temperatures, with distinct bilayer behaviour as observed from their SWAXS data analysis. The calculated bilayer thickness and distribution at T= 25.49 °C obtained from REMD simulation further support the multiple *d*-spacing occurrence in X-ray scattering at T~ 25 °C in the gel phase ($\alpha ManC_{18}$) and lamellar glassy phase ($\alpha ManC_{18:1}$). The corresponding analyses gave two and three preferred tilting angles of the average headgroup, $\langle\theta\rangle$ in the simulated bilayer systems in $\alpha ManC_{18}$ and $\alpha ManC_{18:1}$, respectively, which microscopically correlates to the formation of multiple bilayer thicknesses. The REMD average surface areas of headgroup per lipid (A) for both $\alpha ManC_{18}$ and $\alpha ManC_{18:1}$ are similar in value, but the corresponding plots distribution display other peaks, which supports the existence of multiple *d*-spacings in these incommensurate bilayers, emanating from the competing packing requirements of aliphatic tails and headgroups.

Acknowledgement

This work was supported by the Ministry of Education of Malaysia [600-IRMI/FRGS 5/3 (357/2019)]. We are thankful for the computational facility provided by the National Center for High-Performance Computing of Taiwan used to perform calculations reported in this work. AMF would like to acknowledge the Scottish Government and the Royal Society of Edinburgh, for the award of one SAPHIRE project.

References:

[1] C.-h. Huang, Mixed-chain phospholipids: structures and chain-melting behavior, Lipids 36 (2001) 1077. https://doi.org/10.1007/s11745-001-0818-1.

[2] R.A. Moss, T. Fujita, Y. Okumura, Effect of unsaturation on lipid dynamics within synthetic lipid membranes, Langmuir 7 (1991) 440. https://doi.org/10.1021/la00051a002.

[3] W. Kulig, M. Pasenkiewicz-Gierula, T. Róg, Cis and trans unsaturated phosphatidylcholine bilayers: A molecular dynamics simulation study, Chem. Phys. Lipids 195 (2016) 12. https://doi.org/10.1016/j.chemphyslip.2015.07.002.

[4] M.T. Hyvönen, P.T. Kovanen, Molecular dynamics simulations of unsaturated lipid bilayers: effects of varying the numbers of double bonds, Eur. Biophys. J. 34 (2005) 294. https://doi.org/10.1007/s00249-004-0455-7.

[5] H. Martinez-Seara, T. Rog, M. Pasenkiewicz-Gierula, I. Vattulainen, M. Karttunen, R. Reigada, Effect of double bond position on lipid bilayer properties: insight through atomistic simulations, J. Phys. Chem. B 111 (2007) 11162. https://doi.org/10.1021/jp071894d.

[6] H. Martinez-Seara, T. Róg, M. Pasenkiewicz-Gierula, I. Vattulainen, M. Karttunen, R. Reigada, Interplay of unsaturated phospholipids and cholesterol in membranes: effect of the double-bond position, Biophys. J. 95 (2008) 3295. https://doi.org/10.1529/biophysj.108.138123.

[7] L. Boudière, M. Michaud, D. Petroutsos, F. Rébeillé, D. Falconet, O. Bastien, S. Roy, G. Finazzi, N. Rolland, J. Jouhet, M.A. Block, E. Maréchal, Glycerolipids in photosynthesis: Composition, synthesis and trafficking, Biochim. Biophys. Acta Bioenerg. 1837 (2014) 470. https://doi.org/10.1016/j.bbabio.2013.09.007.

[8] V. Vill, R. Hashim, Carbohydrate liquid crystals: structure–property relationship of thermotropic and lyotropic glycolipids, Curr. Opin. Colloid Interface Sci. 7 (2002) 395. https://doi.org/10.1016/S1359-0294(02)00091-2.

[9] A.G. Cook, J.L. Wardell, N.J. Brooks, J.M. Seddon, A. Martinez-Felipe, C.T. Imrie, Non-symmetric liquid crystal dimer containing a carbohydrate-based moiety, Carbohydr. Res. 360 (2012) 78. https://doi.org/10.1016/j.carres.2012.07.018.

[10] A.G. Cook, A. Martinez-Felipe, N.J. Brooks, J.M. Seddon, C.T. Imrie, New insights into the transitional behaviour of methyl-6-O-(n-dodecanoyl)-α-D-glucopyranoside using variable temperature FTIR spectroscopy and X-ray diffraction, Liq. Cryst. 40 (2013) 1817. https://doi.org/10.1080/02678292.2013.854556.

[11] R. Hashim, H.H.A. Hashim, N.Z.M. Rodzi, R.S.D. Hussen, T. Heidelberg, Branched chain glycosides: Enhanced diversity for phase behavior of easily accessible synthetic glycolipids, Thin Solid Films 509 (2006) 27. https://doi.org/10.1016/j.tsf.2005.09.009.

[12] R.N. Lewis, D.A. Mannock, R.N. Mcelhaney, Membrane lipid molecular structure and polymorphism, Current Topics in Membranes, Elsevier, 1997, p. 25-102.

[13] D.A. Mannock, M.D. Collins, M. Kreichbaum, P.E. Harper, S.M. Gruner, R.N. McElhaney, The thermotropic phase behaviour and phase structure of a homologous series of racemic β-d-galactosyl dialkylglycerols studied by differential scanning calorimetry and X-ray diffraction, Chem. Phys. Lipids 148 (2007) 26. https://doi.org/10.1016/j.chemphyslip.2007.04.004.

[14] M. Hato, H. Minamikawa, K. Tamada, T. Baba, Y. Tanabe, Self-assembly of synthetic glycolipid/water systems, Adv. Colloid Interface Sci. 80 (1999) 233. https://doi.org/10.1016/S0001-8686(98)00085-2.

[15] G.G. Shipley, J.P. Green, B.W. Nichols, The phase behavior of monogalactosyl, digalactosyl, and sulphoquinovosyl diglycerides, Biochim. Biophys. Acta Biomembr. 311 (1973) 531. https://doi.org/10.1016/0005-2736(73)90128-4.

[16] T.T. Chong, R. Hashim, R.A. Bryce, Molecular dynamics simulation of monoalkyl glycoside micelles in aqueous solution: influence of carbohydrate headgroup stereochemistry, J. Phys. Chem. B 110 (2006) 4978. https://doi.org/10.1021/jp056851g.

[17] V. Manickam Achari, H.S. Nguan, T. Heidelberg, R.A. Bryce, R. Hashim, Molecular Dynamics Study of Anhydrous Lamellar Structures of Synthetic Glycolipids: Effects of Chain Branching and Disaccharide Headgroup, J. Phys. Chem. B 116 (2012) 11626. https://doi.org/10.1021/jp302292s.

[18] J. Kapla, B. Stevensson, M. Dahlberg, A. Maliniak, Molecular dynamics simulations of membranes composed of glycolipids and phospholipids, J. Phys. Chem. B 116 (2012) 244. https://doi.org/10.1021/jp209268p.

[19] N.F. Kamalul Aripin, J.M. Heap, R. Piñol, V. Manickam-Achari, A. Martinez-Felipe, Unveiling the hydrogen bonding network in liquid crystalline natural-based glycosides containing polymeric complexes: Experimental and theoretical assessment, Colloids Surf. A Physicochem. Eng. 596 (2020) 124685. https://doi.org/10.1016/j.colsurfa.2020.124685.

[20] R. Hashim, A. Sugimura, H. Minamikawa, T. Heidelberg, Nature-like synthetic alkyl branched-chain glycolipids: a review on chemical structure and self-assembly properties, Liq. Cryst. 39 (2011) 1. https://doi.org/10.1080/02678292.2011.614017.

[21] N.J. Brooks, H.A.A. Hamid, R. Hashim, T. Heidelberg, J.M. Seddon, C.E. Conn, S.M. Mirzadeh Husseini, N.I. Zahid, R.S.D. Hussen, Thermotropic and lyotropic liquid crystalline phases of Guerbet branched-chain -D-glucosides, Liq. Cryst. 38 (2011) 1725. https://doi.org/10.1080/02678292.2011.625689.

[22] W.D. Bennett, D.P. Tieleman, Computer simulations of lipid membrane domains, Biochim. Biophys. Acta Biomembr. 1828 (2013) 1765. https://doi.org/10.1016/j.bbamem.2013.03.004.

[23] D. Shorthouse, G. Hedger, H. Koldsø, M.S. Sansom, Molecular simulations of glycolipids: Towards mammalian cell membrane models, Biochimie 120 (2016) 105. https://doi.org/10.1016/j.biochi.2015.09.033Mini-review.

[24] T. Róg, I. Vattulainen, A. Bunker, M. Karttunen, Glycolipid Membranes through Atomistic Simulations: Effect of Glucose and Galactose Head Groups on Lipid Bilayer Properties, J. Phys. Chem. B 111 (2007) 10146. https://doi.org/10.1021/jp0730895.

[25] H.I. Ingólfsson, M.N. Melo, F.J. Van Eerden, C. Arnarez, C.A. Lopez, T.A. Wassenaar, X. Periole, A.H. De Vries, D.P. Tieleman, S.J. Marrink, Lipid organization of the plasma membrane, J. Am. Chem. Soc. 136 (2014) 14554. https://doi.org/10.1021/ja507832e.

[26] S.E. Feller, A.D. MacKerell, An improved empirical potential energy function for molecular simulations of phospholipids, J. Phys. Chem. B 104 (2000) 7510. https://doi.org/10.1021/jp0007843.

[27] M. Pasenkiewicz-Gierula, K. Baczynski, M. Markiewicz, K. Murzyn, Computer modelling studies of the bilayer/water interface, Biochim. Biophys. Acta Biomembr. 1858 (2016) 2305. https://doi.org/10.1016/j.bbamem.2016.01.024.

[28] M. Kanduč, A. Schlaich, A.H. de Vries, J. Jouhet, E. Maréchal, B. Demé, R.R. Netz, E. Schneck, Tight cohesion between glycolipid membranes results from balanced water–headgroup interactions, Nat. Commun. 8 (2017) 1. https://doi.org/10.1038/ncomms14899.

[29] T.S. Velayutham, H.S. Nguan, B.K. Ng, W.C. Gan, V. Manickam Achari, N.I. Zahid, W.H. Abd Majid, C. Zannoni, R. Hashim, Molecular dynamics of anhydrous glycolipid self-assembly in lamellar and hexagonal phases, Phys. Chem. Chem. Phys. 18 (2016) 15182. https://doi.org/10.1039/c6cp00583g.

[30] Y. Sugita, Y. Okamoto, Replica-exchange molecular dynamics method for protein folding, Chem. Phys. Lett. 314 (1999) 141. https://doi.org/10.1016/S0009-2614(99)01123-9.

[31] K. Kerdpol, J. Kicuntod, P. Wolschann, S. Mori, C. Rungnim, M. Kunaseth, H. Okumura, N. Kungwan, T. Rungrotmongkol, Cavity Closure of 2-Hydroxypropyl-β-Cyclodextrin: Replica Exchange Molecular Dynamics Simulations, Polymers 11 (2019) 145. https://doi.org/10.3390/polym11010145.

[32] J. Razzokov, S. Naderi, P. Van Der Schoot, Nanoscale insight into silk-like protein self-assembly: effect of design and number of repeat units, Phys. Biol. 15 (2018) 066010. https://doi.org/10.1088/1478-3975/aadb5e.

[33] G. Grasso, J.A. Tuszynski, U. Morbiducci, G. Licandro, A. Danani, M.A. Deriu, Thermodynamic and kinetic stability of the Josephin Domain closed arrangement: evidences from replica exchange molecular dynamics, Biol. Direct 12 (2017) 2. https://doi.org/10.1186/s13062-016-0173-y.

[34] R. Niehues, M. Hasilik, G. Alton, C. Körner, M. Schiebe-Sukumar, H.G. Koch, K.-P. Zimmer, R. Wu, E. Harms, K. Reiter, Carbohydrate-deficient glycoprotein syndrome type Ib. Phosphomannose isomerase deficiency and mannose therapy, J. Clin. Investig. 101 (1998) 1414. https://doi.org/10.1172/JCI2350.

[35] B. Kranjčec, D. Papeš, S. Altarac, D-mannose powder for prophylaxis of recurrent urinary tract infections in women: a randomized clinical trial, World J. Urol. 32 (2014) 79. https://doi.org/10.1007/s00345-013-1091-6.

[36] A. Montes-Robledo, R. Baldiris-Avila, J.F. Galindo, D-Mannoside FimH Inhibitors as Non-Antibiotic Alternatives for Uropathogenic Escherichia coli, Antibiotics 10 (2021) 1072. https://doi.org/10.3390/antibiotics10091072.

[37] L. Dehuyser, E. Schaeffer, O. Chaloin, C.G. Mueller, R. Baati, A. Wagner, Synthesis of Novel Mannoside Glycolipid Conjugates for Inhibition of HIV-1 Trans-Infection, Bioconjugate Chem. 23 (2012) 1731. https://doi.org/10.1021/bc200644d.

[38] K. Baczynski, M. Markiewicz, M. Pasenkiewicz-Gierula, Is the tilt of the lipid head group correlated with the number of intermolecular interactions at the bilayer interface?, FEBS Lett. 592 (2018) 1507. https://doi.org/10.1002/1873-3468.13048.

[39] J. Bolze, V. Kogan, D. Beckers, M. Fransen, High-performance small-and wide-angle X-ray scattering (SAXS/WAXS) experiments on a multi-functional laboratory goniometer platform with easily exchangeable X-ray modules, Rev. Sci. Instrum. 89 (2018) 085115. https://doi.org/10.1063/1.5041949.

[40] M.A. Kiselev, D. Lombardo, Structural characterization in mixed lipid membrane systems by neutron and X-ray scattering, Biochim. Biophys. Acta Gen. Subj. 1861 (2017) 3700. https://doi.org/10.1016/j.bbagen.2016.04.022.

[41] H. Grubmller, Predicting slow structural transitions in macromolecular systems: Conformational flooding, Phys. Rev. E 52 (1995) 2893. https://doi.org/10.1103/PhysRevE.52.2893.

[42] R.H. Swendsen, J.-S. Wang, Replica Monte Carlo simulation of spin-glasses, Phys. Rev. Lett. 57 (1986) 2607. https://doi.org/10.1016/0378-4371(92)90465-3.

[43] K. Hukushima, K. Nemoto, Exchange Monte Carlo Method and Application to Spin Glass Simulations, Exchange Monte Carlo Method and Application to Spin Glass Simulations 65 (1996) 1604. 10.1143/JPSJ.65.1604.

[44] C. Yang, H. Kim, Y. Pak, Improving Temperature Generator in Parallel Tempering Simulation in the NPT Condition, J. Chem. Theory Comput. 16 (2020) 1827. https://doi.org/10.1021/acs.jctc.9b00984.

[45] D. Van Der Spoel, E. Lindahl, B. Hess, G. Groenhof, A.E. Mark, H.J.C. Berendsen, GROMACS: Fast, flexible, and free, J. Comput. Chem. 26 (2005) 1701. https://doi.org/10.1002/jcc.20291.

[46] B. Hess, C. Kutzner, D. van der Spoel, E. Lindahl, GROMACS 4: Algorithms for Highly Efficient, Load-Balanced, and Scalable Molecular Simulation, J. Chem. Theory Comput. 4 (2008) 435. https://doi.org/10.1021/ct700301q.

[47] M. Parrinello, A. Rahman, Polymorphic transitions in single crystals: A new molecular dynamics method, J. Appl. Phys. 52 (1981) 7182. https://doi.org/10.1063/1.328693.

[48] R. Hashim, Computer Modeling of Liquid Crystals, Understanding Soft Condensed Matter via Modeling and Computation, p. 297-337.

[49] E. Schneck, F. Sedlmeier, R.R. Netz, Hydration repulsion between biomembranes results from an interplay of dehydration and depolarization, Proc. Natl. Acad. Sci. U.S.A. 109 (2012) 14405. https://doi.org/10.1073/pnas.1205811109.

[50] M. Doxastakis, V.G. Sakai, S. Ohtake, J. Maranas, J. De Pablo, A molecular view of melting in anhydrous phospholipidic membranes, Biophys. J. 92 (2007) 147. https://doi.org/10.1529/biophysj.106.089631.

[51] W.F. Van Gunsteren, H.J.C. Berendsen, A Leap-frog Algorithm for Stochastic Dynamics, Mol. Simul. 1 (1988) 173. https://doi.org/10.1080/08927028808080941.

[52] B. Hess, H. Bekker, H.J.C. Berendsen, J.G.E.M. Fraaije, LINCS: A linear constraint solver for molecular simulations, J. Comput. Chem. 18 (1997) 1463. https://doi.org/10.1002/(SICI)1096-987X(199709)18:12<1463::AID-JCC4>3.0.CO;2-H.

[53] U. Essmann, L. Perera, M.L. Berkowitz, T. Darden, H. Lee, L.G. Pedersen, A smooth particle mesh Ewald method, J. Chem. Phys. 103 (1995) 8577. https://doi.org/10.1063/1.470117.

[54] K.A. Ishak, N.I. Zahid, T.S. Velayutham, M.S.M. Annuar, R. Hashim, Effects of lipid packing and intermolecular hydrogen bond on thermotropic phase transition of stearyl glucoside, J. Mol. Liq. 281 (2019) 20. https://doi.org/10.1016/j.molliq.2019.02.075.

[55] Y. Zhang, L. Chen, X. Wu, Thermotropic liquid crystalline and surface-active properties of n-alkyl α-D-mannopyranosides, J. Mol. Liq. 269 (2018) 947. https://doi.org/10.1016/j.molliq.2018.02.017.

[56] H.M. von Minden, K. Brandenburg, U. Seydel, M.H. Koch, V. Garamus, R. Willumeit, V. Vill, Thermotropic and lyotropic properties of long chain alkyl glycopyranosides. Part II. Disaccharide headgroups, Chem. Phys. Lipids 106 (2000) 157. https://doi.org/10.1016/S0009-3084(00)00151-1.

[57] V. Vill, H.M. von Minden, M.H. Koch, U. Seydel, K. Brandenburg, Thermotropic and lyotropic properties of long chain alkyl glycopyranosides. Part I: monosaccharide headgroups, Chem. Phys. Lipids 104 (2000) 75. https://doi.org/10.1016/S0009-3084(99)00119-X.

[58] R. Hori, Y. Ikegami, Studies on Carbohydrate Derivatives. V Syntheses of Alkyl Galactosides and Alkyl Glucosides, Yakugaku Zasshi 79 (1959) 80. https://doi.org/10.1248/yakushi1947.79.1_80.

[59] R. Hashim, N.I. Zahid, T.S. Velayutham, N.F.K. Aripin, S. Ogawa, A. Sugimura, Dry Thermotropic Glycolipid Self-Assembly:A Review, J. Oleo Sci. 67 (2018) 651. https://doi.org/10.5650/jos.ess17261.

[60] C.A. Ericsson, L.C. Ericsson, V. Kocherbitov, O. Soderman, S. Ulvenlund, Thermotropic phase behaviour of long-chain alkylmaltosides, Phys. Chem. Chem. Phys. 7 (2005) 2970. https://doi.org/10.1039/b502922h.

[61] J. Seddon, R. Templer, Polymorphism of lipid-water systems, Handbook of biological physics, Elsevier, 1995, p. 97-160.

[62] F.C. Wang, A.G. Marangoni, Advances in the application of food emulsifier α-gel phases: Saturated monoglycerides, polyglycerol fatty acid esters, and their derivatives, J. Colloid Interface Sci. 483 (2016) 394. https://doi.org/10.1016/j.jcis.2016.08.012.

[63] A. Alfutimie, R. Curtis, G.J.T. Tiddy, Gel phase (Lβ) formation by mixed saturated and unsaturated monoglycerides, Colloids Surf. A Physicochem. Eng. Asp. 456 (2014) 286. https://doi.org/10.1016/j.colsurfa.2014.05.012.

[64] V. Kocherbitov, O. Soderman, Glassy crystalline state and water sorption of alkyl maltosides, Langmuir 20 (2004) 3056. https://doi.org/10.1021/la035553c.

[65] A. Martinez-Felipe, T.S. Velayutham, N.F.K. Aripin, M. Yusoff, E. Farquharson, R. Hashim, Glycolipids from natural sources: dry liquid crystal properties, hydrogen bonding and molecular mobility of Palm Kernel oil mannosides, Liq. Cryst. 47 (2020) 1180. https://doi.org/10.1080/02678292.2020.1750719.

[66] M.R. Rich, Conformational analysis of arachidonic and related fatty acids using molecular dynamics simulations, Biochim. Biophys. Acta Mol. Cell Res. 1178 (1993) 87. https://doi.org/10.1016/0167-4889(93)90113-4.

[67] V. ManickamAchari, R.A. Bryce, R. Hashim, Conformational dynamics of dry lamellar crystals of sugar based lipids: An atomistic simulation study, PLoS One 9 (2014) e101110. https://doi.org/10.1371/journal.pone.0101110.

[68] T. Nagai, R. Ueoka, Y. Okamoto, Phase Behavior of a Lipid Bilayer System Studied by a Replica-Exchange Molecular Dynamics Simulation, J. Phys. Soc. Japan 81 (2012) 024002. https://doi.org/10.1143/JPSJ.81.024002.

[69] S. Ahmadi, V. Manickam Achari, H. Nguan, R. Hashim, Atomistic simulation studies of the alpha/beta-glucoside and galactoside in anhydrous bilayers: effect of the anomeric and epimeric configurations, J. Mol. Model. 20 (2014) 2165. https://doi.org/10.1007/s00894-014-2165-0.

[70] H. Nguan, S. Ahmadi, R. Hashim, Molecular dynamics simulations of the lyotropic reverse hexagonal (HII) of Guerbet branched-chain beta-D-glucoside, Phys. Chem. Chem. Phys. 16 (2014) 324. https://doi.org/10.1039/c3cp52385c.

[71] A. Dickey, R. Faller, Examining the contributions of lipid shape and headgroup charge on bilayer behavior, Biophys. J. 95 (2008) 2636. https://doi.org/10.1529/biophysj.107.128074.

[72] K. Baczynski, M. Markiewicz, M. Pasenkiewicz-Gierula, A computer model of a polyunsaturated monogalactolipid bilayer, Biochimie 118 (2015) 129. https://doi.org/10.1016/j.biochi.2015.09.007.

[73] O. Guvench, E. Hatcher, R.M. Venable, R.W. Pastor, A.D. MacKerell, CHARMM Additive All-Atom Force Field for Glycosidic Linkages between Hexopyranoses, J. Chem. Theory Comput. 5 (2009) 2353. https://doi.org/10.1021/ct900242e.

[74] A. Martinez-Felipe, Z. Lu, P.A. Henderson, S.J. Picken, B. Norder, C.T. Imrie, A. Ribes-Greus, Synthesis and characterisation of side chain liquid crystal copolymers containing sulfonic acid groups, Polymer 53 (2012) 2604. https://doi.org/10.1016/j.polymer.2012.02.029.

[75] J.-W. Lee, J.-I. Jin, M.F. Achard, F. Hardouin, Incommensurability induced by intermolecular hydrogen bonding, Liq. Cryst. 28 (2001) 663. https://doi.org/10.1080/02678290010028726.

[76] C.T. Imrie, P.A. Henderson, Liquid crystal dimers and higher oligomers: between monomers and polymers, Chem. Soc. Rev. 36 (2007) 2096. https://doi.org/10.1039/b714102e.

[77] J. Prost, P. Barois, Polymorphism in polar mesogens. II-Theoretical aspects, J. Chim. Phys. 80 (1983) 65. https://doi.org/10.1051/jcp/1983800065.

[78] F. Hardouin, A. Levelut, M. Achard, G. Sigaud, Polymorphisme des substances mésogčnes a molécules polaires. I. Physico-chimie et structure, J. Chim. Phys. 80 (1983) 53. https://doi.org/10.1051/jcp/1983800053.

[79] C. Böhm, H. Möhwald, L. Leiserowitz, J. Als-Nielsen, K. Kjaer, Influence of chirality on the structure of phospholipid monolayers, Biophys. J. 64 (1993) 553. https://doi.org/10.1016/S0006-3495(93)81386-9.

[80] M. Scheringer, R. Hilfer, K. Binder, Orientational ordering in lipid monolayers: A two-dimensional model of rigid rods grafted onto a lattice, J. Chem. Phys. 96 (1992) 2269. https://doi.org/10.1063/1.462077.

[81] K. Hristova, S.H. White, Determination of the hydrocarbon core structure of fluid dioleoylphosphocholine (DOPC) bilayers by x-ray diffraction using specific bromination of the double-bonds: effect of hydration, Biophys. J. 74 (1998) 2419. https://doi.org/10.1016/S0006-3495(98)77950-0.

[82] C.-J. Högberg, A.P. Lyubartsev, A molecular dynamics investigation of the influence of hydration and temperature on structural and dynamical properties of a dimyristoylphosphatidylcholine bilayer, J. Phys. Chem. B 110 (2006) 14326. https://doi.org/10.1021/jp0614796.

[83] U. Lehnert, V. Réat, M. Weik, G. Zaccai, C. Pfister, Thermal motions in bacteriorhodopsin at different hydration levels studied by neutron scattering: correlation with kinetics and light-induced conformational changes, Biophys. J. 75 (1998) 1945. https://doi.org/10.1016/S0006-3495(98)77635-0.

[84] M. Trapp, T. Gutberlet, F. Juranyi, T. Unruh, B. Demé, M. Tehei, J. Peters, Hydration dependent studies of highly aligned multilayer lipid membranes by neutron scattering, J. Chem. Phys. 133 (2010) 10B615. https://doi.org/10.1063/1.3495973.

[85] A. Tardieu, V. Luzzati, F.C. Reman, Structure and polymorphism of the hydrocarbon chains of lipids: A study of lecithin-water phases, J. Mol. Biol. 75 (1973) 711. https://doi.org/10.1016/0022-2836(73)90303-3.

[86] L. Dahbi, M. Arbel-Haddad, P. Lesieur, C. Bourgaux, M. Ollivon, A long ripple phase in DLPC–decylglucoside mixture evidenced by synchrotron SAXS coupled to DSC, Chem. Phys. Lipids 139 (2006) 43. https://doi.org/10.1016/j.chemphyslip.2005.10.002.

Declaration of interests

☐ The authors declare that they have no known competing financial interests or personal relationships that could have appeared to influence the work reported in this paper.

☒ The authors declare the following financial interests/personal relationships which may be considered as potential competing interests:

Nurul Fadhilah Kamalul Aripin reports financial support was provided by Malaysia Ministry of Higher Education.

Highlights:

• Phase behaviours of long-chain mannosides with stearyl and monounsaturated oleyl hydrocarbon chains.

• From the SWAXS, these mannosides exhibited multiple d-spacing bilayer structures – incommensurate phases.

• The multiple headgroup tilt angles, $\langle\theta\rangle$ from the REMD simulations explained the observed incommensurate bilayer structures.

• Different tilting angles of the headgroup will correspondingly give different surface areas per lipid.